nature COMMUNICATIONS

ARTICLE

DOI: 10.1038/s41467-017-01166-3 OPEN

Carbon dioxide capture and conversion by an acid-base resistant metal-organic framework

Linfeng Liang[1,2], Caiping Liu[1], Feilong Jiang[1], Qihui Chen[1], Linjie Zhang[1], Hui Xue[1], Hai-Long Jiang[2,3], Jinjie Qian[4], Daqiang Yuan[1] & Maochun Hong[1,2]

Considering the rapid increase of CO_2 emission, especially from power plants, there is a constant need for materials which can effectively eliminate post-combustion CO_2 (the main component: $CO_2/N_2 = 15/85$). Here, we show the design and synthesis of a Cu(II) metal-organic framework (**FJI-H14**) with a high density of active sites, which displays unusual acid and base stability and high volumetric uptake (171 $cm^3\,cm^{-3}$) of CO_2 under ambient conditions (298 K, 1 atm), making it a potential adsorbing agent for post-combustion CO_2. Moreover, CO_2 from simulated post-combustion flue gas can be smoothly converted into corresponding cyclic carbonates by the **FJI-H14** catalyst. Such high CO_2 adsorption capacity and moderate catalytic activity may result from the synergistic effect of multiple active sites.

[1] State Key Laboratory of Structure Chemistry, Fujian Institute of Research on the Structure of Matter, Chinese Academy of Sciences, Fuzhou, Fujian 350002, China. [2] Department of Chemistry, University of Science and Technology of China, Hefei, Anhui 230026, China. [3] Hefei National Laboratory for Physical Sciences at the Microscale, Hefei, Anhui 230026, China. [4] College of Chemistry and Materials Engineering, Wenzhou University, Wenzhou 325035, China. Correspondence and requests for materials should be addressed to Q.C. (email: chenqh@fjirsm.ac.cn) or to D.Y. (email: ydq@fjirsm.ac.cn) or to M.H. (email: hmc@fjirsm.ac.cn)

Due to the dependence on fossil fuels to meet the world's growing energy demand, the concentration of CO_2 in the atmosphere has increased from 310 p.p.m. to over 380 p.p.m. during the last half century, and it continues to rise[1–3]. Some 60% of the total CO_2 emission worldwide is attributable to electricity generation[4]. The installation of effective CO_2 capture systems that can selectively remove the CO_2 component of the exhaust gas emitted by coal- or gas-fired power plants would extremely reduce the global annual emissions. Current technologies involving aqueous amine absorbents for the capture of CO_2 from a gas mixture are usually themselves significant consumers of energy and a source of corrosion problems in equipment[5–7]. Thus, exploration of new materials that can selectively and efficiently eliminate combustion-generated CO_2 is urgent.

Due to their large capacity for the adsorption of gases and their chemical tunability[8–21], the emerging porous metal-organic frameworks (MOFs) could serve as promising cost-effective and efficient materials for CO_2 capture and separation, but development of practically useful MOF materials for CO_2 capture directly from power plants remains a challenge. The flue gas generated from coal-fired power plant, released at a total pressure of approximately 1 atm., contains 15–16% CO_2, 73–77% N_2, 5–7% H_2O, 3–4% O_2 and a small amount of acid gas[22–24]. An ideal MOF material for CO_2 capture should exhibit extraordinarily high CO_2 uptake and selectivity at ambient pressures; furthermore, it should also be resistant to water and acid gas, can be prepared on a large scale and is reusable. Moreover, in terms of practical applications, high volumetric CO_2 adsorption capacity seems even more important than gravimetric CO_2 adsorption capacity, since the capture and separation of post-combustion CO_2 is often carried out in a fixed-bed reactor[5].

Generally, open metal sites (OMS) and Lewis basic sites (LBS) are favorable for interaction with CO_2 and various types of OMS and LBS have been introduced into MOFs in an effort to improve their adsorption capacity[25–32]. To adsorb CO_2 effectively under ambient conditions, one would seek to prepare an MOF with high densities of OMS and LBS, in which the OMS and LBS could synergistically capture CO_2 molecules in the pores. Such a potential synergy effect from the OMS and LBS can improve the adsorption capacity more effectively than a single OMS or LBS.

In this paper, we describe the design and synthesis of a Cu(II)-MOF, **FJI-H14** with a high density of OMS and LBS, which shows extraordinary high volumetric uptake of CO_2 at ambient conditions and excellent selectivity for CO_2 over N_2. Remarkably, it is highly stable in a water and acid/base environment and can be reused without loss of adsorption capacity; furthermore, it can be easily synthesized in large quantities. Experiments with simulated post-combustion flue gas have shown that **FJI-H14** can smoothly catalyze the chemical transformation of CO_2 into the corresponding cyclic carbonates.

Results

Synthesis and structure analysis. The reaction of 2,5-di(1*H*-1,2,4-triazol-1-yl)terephthalic acid (H_2BTTA, Fig. 1a) with Cu $(NO_3)_2$ in H_2O at 120 °C for 3 days affords rod-shaped blue crystals of **FJI-H14** ($[Cu(BTTA)H_2O]_n \cdot 6nH_2O$) in 73% yield. Single-crystal X-ray structure analysis shows that **FJI-H14** crystallizes in trigonal space group *R*-3 (for more details see Supplementary Table 1). The crystallographic asymmetric unit contains one $BTTA^{2-}$ligand, one Cu(II) ion and one coordinate water. As shown in Fig. 1b, each Cu(II) ion has a square-pyramidal coordination geometry, and is surrounded by two imine N atoms from two different 1,2,4-triazole groups and two O atoms from two different carboxylate groups in the equatorial plane, together with one O atom of the water molecule in the vertex (Supplementary Fig. 1). Topologically, the Cu(II) ion is a planar 4-connected node, further linked by four tetradentate $BTTA^{2-}$ ligands into a three-dimensional network with Kagome-like **USF** topology (Fig. 1d). Consequently, there are hexagonal one-dimensional channels along the *c* direction (Fig. 1c). The pore limiting diameter and the maximum pore diameter predicted by the program Poreblazer[33] for the fully evacuated **FJI-H14** are 5.95 and 7.62 Å, respectively. The evacuated **FJI-H14** has a theoretical porosity of 44.4% according to PLATON calculations with a probe radius of 1.65 Å. **FJI-H14** has a total concentration of active sites as high as 9.22 mol l^{-1} (the total of Cu (II) OMS is 3.07 mol l^{-1} and free N LBS is 6.15 mol l^{-1}), which is higher than in many well-known MOFs for CO_2 capture (Supplementary Table 2).

Stability. The flue gas from power plants contains moisture and acid gas, suggesting that the practical adsorbents of post-combustion CO_2 should be sufficiently stable toward heat, water and acid. This led us to investigate both the chemical stability and thermal stability of **FJI-H14** before the CO_2 adsorption test. Powder X-ray diffraction pattern (PXRD) analyses reveal that **FJI-H14** is very stable not only in boiling water but also in both acid and base environments at pH = 2 to pH = 12 and at temperatures as high as 373 K (Fig. 2a). However, the framework of **FJI-H14** collapses when it is immersed for 24 h in solution at pH = 1 or pH = 13 (Supplementary Fig. 2). Thermogravimetric analysis (TGA) studies (Supplementary Fig. 3) indicate that the as-synthesized **FJI-H14** sample is thermally stable up to 230 °C, and this is confirmed by temperature-dependent PXRD studies (Fig. 2b and Supplementary Fig. 4). Generally, MOFs based on Cu ions and organic carboxylates are usually subject to hydrolysis in the presence of moisture and only a few known MOFs show such excellent chemical stability[16, 34–38]. The unusual chemical stability of **FJI-H14** may result from its unique structure because the penta-coordinated Cu(II) ion subunit should be more stable than

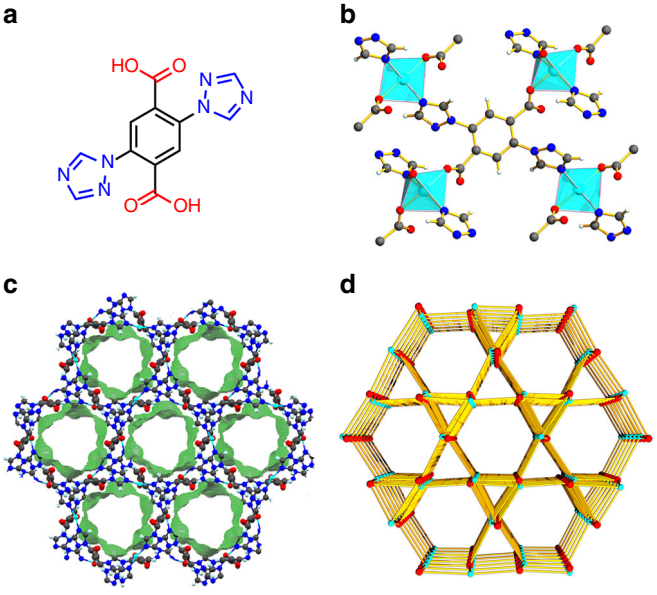

Fig. 1 Structural illustration of FJI-H14. **a** The selected ligand H_2BTTA for the construction of **FJI-H14**. **b** The coordination environment of the Cu(II) ions as four-connected nodes and BTTA also as a four-connected node. **c** The one-dimensional nanoporous channels along the crystallographic *c* direction. **d** The framework of **USF** topology. (Cu atom, cyan; C atom, gray; O atom, red; N atom, blue; H atom, white)

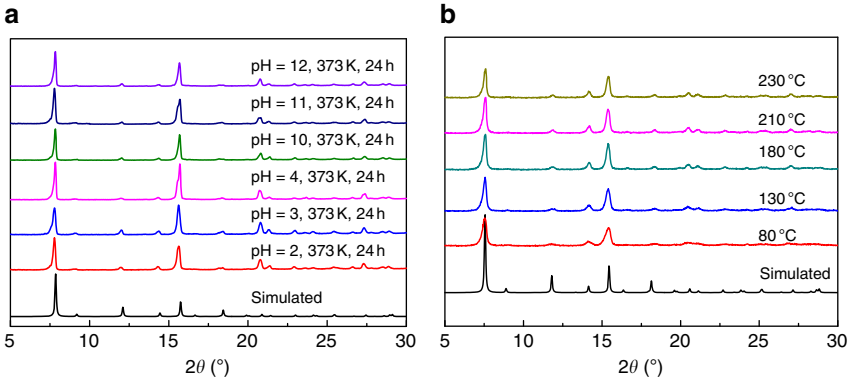

Fig. 2 Stability of FJI-H14. **a** PXRD patterns after treatment with boiling water, acid/base environment from pH = 2 to 12 at 373 K. **b** Temperature-dependent PXRD patterns

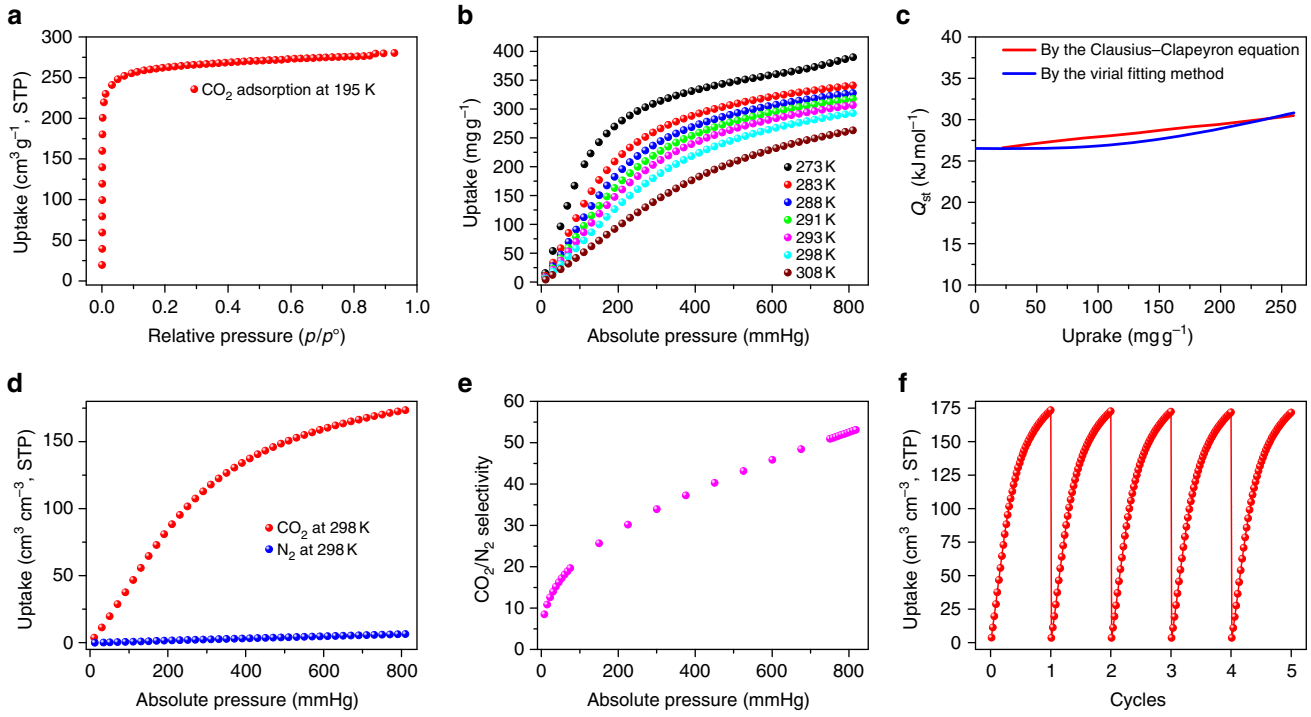

Fig. 3 Experimental CO_2 adsorption by FJI-H14. **a** CO_2 adsorption isotherm for **FJI-H14** at 195 K. **b** CO_2 adsorption isotherm for **FJI-H14** at 273, 283, 288, 291, 293, 298 and 308 K. **c** The isosteric heat of CO_2 adsorption (Q_{st}) for **FJI-H14** calculated by the Clausius–Clapeyron equation and the Virial fitting method. **d** N_2 and CO_2 adsorption isotherms for **FJI-H14** at 298 K. **e** CO_2/N_2 selectivity for the 15/85 CO_2/N_2 mixture at 298 K. **f** Cycles of CO_2 adsorption for **FJI-H14** at 298 K

traditional paddle-wheel structure due to the Cu–N coordination interaction, which is stronger than the Cu–O interaction. Furthermore, the abundant free N atoms could also prevent the destruction caused by acids.

Porosity and CO_2 adsorption capacity. The **FJI-H14** sample for adsorption testing was pre-activated under dynamic vacuum at 100 °C for 10 h after exchanged by acetone for 3 days. PXRD data displayed that the crystallinity was retained after activation (Supplementary Fig. 5). N_2 adsorption at 77 K was much lower than expected (Supplementary Fig. 6), and consequently, the porosity of activated **FJI-H14** was examined by CO_2 adsorption experiments at 195 K. A CO_2 uptake of 279 $cm^3\ g^{-1}$ was obtained (Fig. 3a), corresponding to a formula $[Cu(BTTA)]_n{\cdot}4.5nCO_2$. A phenomenon that restricted N_2 uptake at 77 K but supported type-I CO_2 uptake at 195 K has been observed in several reported MOF materials (Supplementary Table 3). However, **FJI-H14** has a low N_2 uptake of 170 $cm_3\ g^{-1}$ at 77 K and 1 atm, which is different from the reported MOFs which exhibit almost zero N_2 adsorption at 77 K. The much lower N_2 adsorption at 77 K of **FJI-H14** may be a consequence of the relatively narrow pores in **FJI-H14** being easily blocked by the relatively large N_2 molecule at 77 K, so hindering further diffusion of N_2 into the framework of **FJI-H14**. The typical type-I isotherm observed indicates that only micropores are formed in the framework of activated **FJI-H14**. The Brunauer–Emmett–Teller (BET) -specific surface area of **FJI-H14** is calculated to be 904 $m^2\ g^{-1}$ and its Langmuir-specific surface area is 1004 $m^2\ g^{-1}$. The total pore volume estimated from the experimental CO_2 isotherm is 0.45 $cm^3\ g^{-1}$ at $P/P_0 = 0.92$,

which is slightly higher than the theoretical value of 0.39 $cm^3 g^{-1}$ derived from the solvent accessible volume and the crystal density through PLATON calculations with a probe radius of 1.65 Å. The comparable values of the pore volume indicate that the activated **FJI-H14** remains permanently porous.

The incorporation of high porosity and the high concentration of open active sites in the framework are expected to lead to high CO_2 uptake. Indeed, activated **FJI-H14** exhibits remarkable CO_2 volumetric adsorption capacities of 171 $cm^3 cm^{-3}$ at 298 K and 1 atm (Fig. 3d), and the capacity is only lower than that of MAF-X25ox (203 $cm^3 cm^{-3}$)[36], MAF-X27ox (196 $cm^3 cm^{-3}$)[36] and Co_2(dobdc) (184 $cm^3 cm^{-3}$) under the same conditions[36, 39], exceeding that in almost all well-known MOFs such as Mg-MOF-74 (162 $cm^3 cm^{-3}$)[6, 40], UTSA-16 (160 $cm^3 cm^{-3}$)[6, 41], SIFSIX-2-Cu-i (151 $cm^3 cm^{-3}$)[42], MPM-1-TIFSIX (115.7 $cm^3 cm^{-3}$)[43], Bio-MOF-11(113 $cm^3 cm^{-3}$)[6, 44], Cu-tdpat(103 $cm^3 cm^{-3}$)[6, 45] and Mmen–CuBTTri (83 $cm^3 cm^{-3}$)[6, 30] (Supplementary Table 2). The formula of CO_2 adsorbed **FJI-H14** at room temperature is $[Cu(BTTA)]_n \cdot 2.4nCO_2$ and there is a 53% CO_2 occupancy at room temperature compared with the maximal uptake at 195 K, which is rather high compared with reported MOFs such as SMT-1 (27%)[46], [Cu(L)] (31%)[47] and MPM-1-Cl (29%)[43]. It should be noted that although volumetric adsorption capacity is more practical for stationary CO_2 capture and separation applications, the gravimetric adsorption capacity is also an important parameter for CO_2 capture. Although the gravimetric CO_2 uptake of **FJI-H14** (146 $cm^3 g^{-1}$) is lower than that of Mg-MOF-74 (176 $cm^3 g^{-1}$) due to the considerably lighter weight of Mg[40], it can be comparable to that in other familiar MOF materials such as MAF-X25ox (160 $cm^3 g^{-1}$)[36], [Co_2(dobdc)] (154 $cm^3 g^{-1}$)[39] or MAF-X27ox (150 $cm^3 g^{-1}$)[36]. Another challenging issue is the uptake of CO_2 at low pressure, which can be highly improved by chemisorption due to the stronger interactions. For instance, the hydrazine functionalized MOF [Mg_2(dobdc)(N_2H_4)$_{1.8}$] (137 $cm^3 cm^{-3}$) developed by Zhang et al. shows the highest volumetric CO_2 adsorption capacities at 298 K and 0.15 bar[31], and the second highest is MAF-X27ox (124 $cm^3 cm^{-3}$)[36], which was also prepared by Zhang et al. Based on physisorption, **FJI-H14** displays a volumetric capacity of 60 $cm^3 cm^{-3}$ at 298 K and 0.15 atm, which makes it comparable to SIFSIX-2-Cu-i (63 $cm^3 cm^{-3}$). In order to evaluate the affinity of the pore surface of activated **FJI-H14** toward CO_2, the isosteric heat of adsorption (Q_{st}) of activated **FJI-H14** was calculated using the Clausius–Clapeyron equation based on the CO_2 isotherms at seven different temperatures without data fitting (Fig. 3b, Supplementary Fig. 7 and Supplementary Table 4). As shown in Fig. 3c, the Q_{st} at low coverage is 26.6 kJ mol^{-1} and then slightly increases to 30.5 kJ mol^{-1} with CO_2 loading increasing to 260 mg g^{-1}. The Q_{st} with an increasing slope is unusual[9, 36, 43, 48], and reveals the possible formation of CO_2 clusters inside the pores. Such phenomena have been previously observed in other porous MOFs materials[41, 49]. The Q_{st}, confirmed by the Virial fitting method[50], also slowly increases from 26.5 to 30.8 kJ mol^{-1} with increasing CO_2 loading from lower coverage to 260 mg g^{-1} (Fig. 3c and Supplementary Fig. 8). Such similar trends in the two methods confirm the unusual increasing slope in Q_{st}.

Because flue gas from power plants contains a large amount of N_2, the CO_2/N_2 selectivity is a crucial parameter in CO_2 capture applications. For comparison, N_2 sorption isotherms were also measured at 298 K, and showed an uptake of 6.5 $cm^3 cm^{-3}$ at 1 atm (Fig. 3d). By the ideal adsorbed solution theory (IAST)[51], the CO_2/N_2 selectivity for the 15/85 CO_2/N_2 mixture at 1 atm is calculated to be 51 at 298 K (Fig. 3e). The highly selective adsorption of CO_2 over N_2 further suggests that the densely populated open active sites in the framework have a positive effect on CO_2 adsorption. The possibility of reuse of an adsorbent is also an important aspect of the practical application. Further research demonstrates that activated **FJI-H14** can be recycled without losing its adsorption capacity. Even after five cycles, it still maintains 100% adsorption capacity as shown in Fig. 3f, indicating that **FJI-H14** is highly suitable for CO_2 capture.

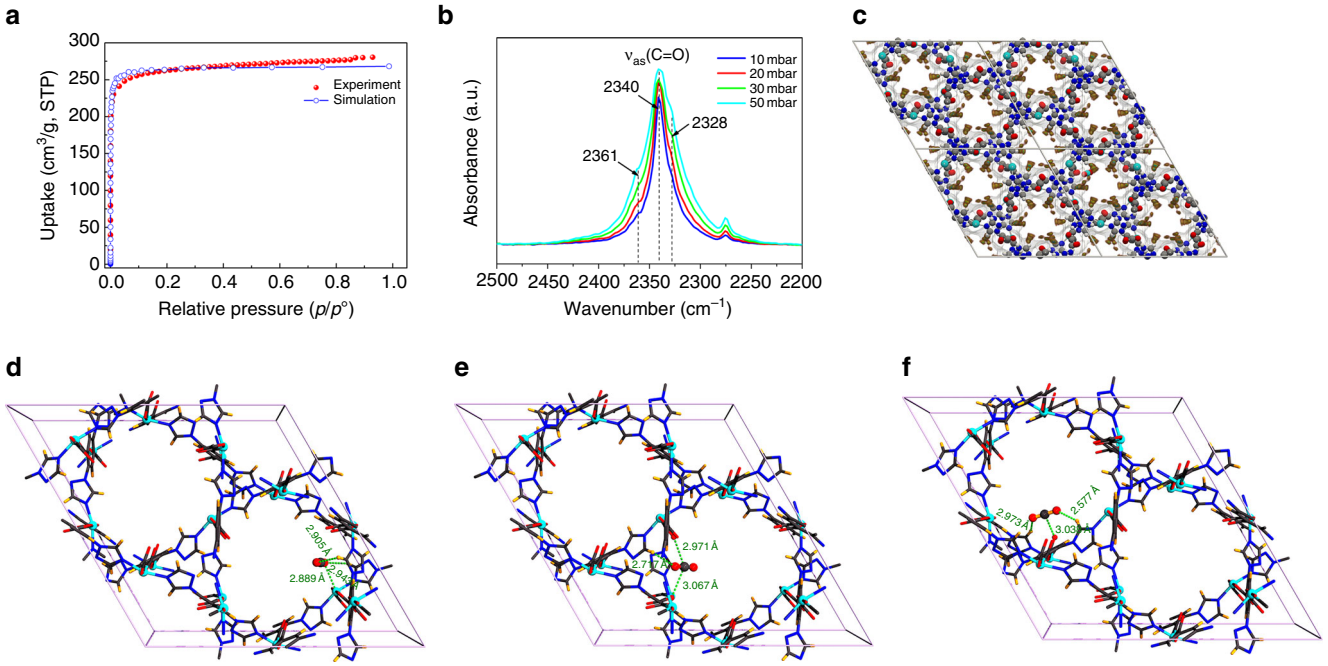

Fig. 4 Mechanism of CO_2 adsorption of FJI-H14. **a** Experimental and simulated excess CO_2 adsorption isotherms at 195 K. **b** Background-subtracted FTIR spectra of CO_2 adsorbed on **FJI-H14** at decreasing equilibrium pressure. **c** Density picture of adsorbed CO_2 (1 CO_2 at 273 K), which is shown as a volume rendered mode. **d**–**f** represent three preferential CO_2 locations in **FJI-14** obtained from GCMC simulation and DFT optimization

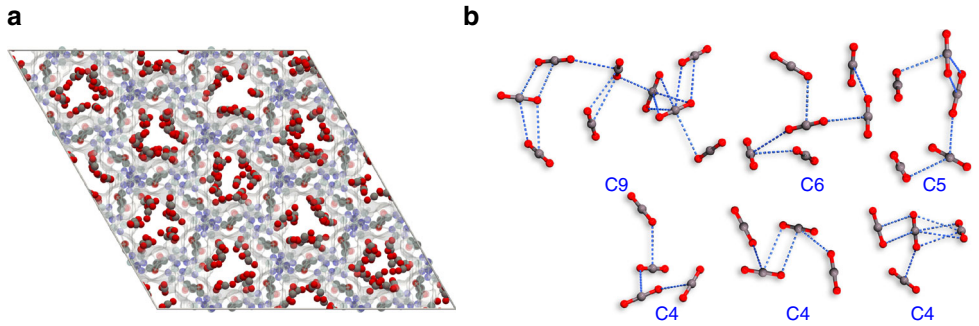

Fig. 5 The snapshot for CO_2-loaded FJI-H14. **a** The snapshot of CO_2 adsorption for **FJI-H14** at 11.2 kPa and 273.15 K calculated using the GCMC method. **b** The representative CO_2 clusters including nine (C9), six (C6), five (C5) and four (C4) CO_2 molecules. The blue dashed line represents weak interactions between neighboring CO_2 molecules with a short C···O separation (from 2.71 to 3.50 Å) for adjacent CO_2 molecules

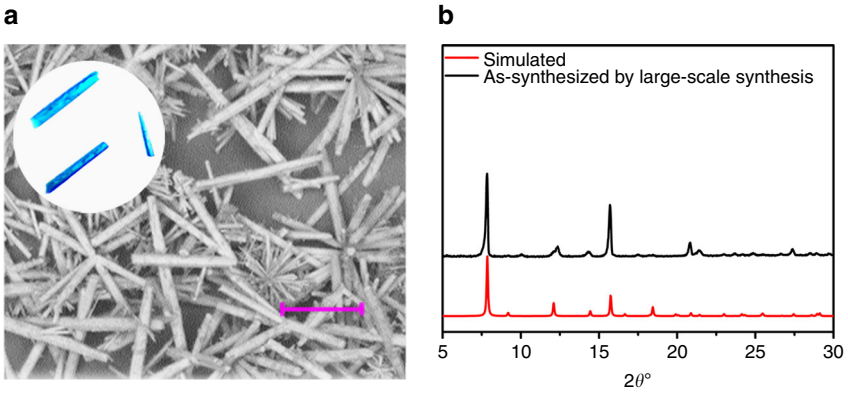

Fig. 6 Large-scale synthesis of FJI-H14 microcrystals. **a** Morphology comparison between SEM image of **FJI-H14** microcrystals and of **FJI-H14** single crystals (inset). Scale bars, 10 μm. **b** PXRD patterns comparison: black represents simulated **FJI-H14**; red represents **FJI-H14** microcrystals

Revealing the CO_2 adsorption sites in FJI-H14. The extraordinary CO_2 capture performance of **FJI-H14** under ambient conditions has motivated us to rationalize the crucial factors supporting the high CO_2 adsorption capacity. To understand the sorption behavior of **FJI-H14**, both grand canonical Monte Carlo (GCMC) simulations and density functional theory (DFT) calculations have been carried out and are shown in Fig. 4. The GCMC simulations show that the theoretical CO_2 adsorption isotherms of **FJI-H14** are basically consistent with the experimental data at different temperatures (195, 273 and 298 K) (Fig. 4a, Supplementary Fig. 9). The simulated CO_2 concentration loaded into **FJI-H14** is about 4.3, 3.1 and 2.5 CO_2 per ligand molecule at 195, 273 and 298 K, respectively. These figures are close to the experimental values of 4.5, 3.1 and 2.4 CO_2 per ligand molecule at 195, 273 and 298 K. As shown in Fig. 4c, the adsorbed CO_2 molecules at low coverage prefer to locate the corners of hexagonal channels. Combining the density plots and a snapshot of the adsorbed CO_2 molecules, three typical preferential CO_2 adsorption sites can be observed. These three adsorption sites were further optimized by DFT methods using the Dmol[3] module. Site I (Fig. 4d) shows that CO_2 molecules prefer to coordinate with open Cu(II) ions through Cu–O interaction, with a Cu–O distance of about 2.889 Å, and each copper site binding only one CO_2[52]. In Site II (Fig. 4e), the two closest C–O distances are about 2.971 and 3.067 Å, indicating that O atoms of carboxyl group could also interact as a Lewis base with CO_2. It is also interesting to find that positively charged H atoms could further promote CO_2 adsorption, with the shortest O-H distances about 2.577 Å as shown in Site III (Fig. 4f). The calculated static CO_2 binding energy of the above three different preferential CO_2 adsorption sites are ~43.71, 38.94, 32.82 kJ mol^{-1}, respectively, indicating that the open copper sites could play a leading role in CO_2 adsorption.

The simulated Q_{st} from the GCMC simulations can be used to deduce the information on Q_{st} with an increasing slope for **FJI-H14**. As shown in Supplementary Fig. 10, the simulated Q_{st} of 30.7–34.6 kJ mol^{-1} is slightly larger than suggested by experimental results and has a uniformly increasing trend with increasing CO_2 loading. The contribution of the CO_2···Framework interaction to the total Q_{st} decreases slightly with increasing loading, which is reasonable because CO_2 molecules first occupied the more active sites. However, the contribution from the CO_2···CO_2 interactions shows a tendency to increase significantly from 0 to 7.0 kJ mol^{-1}, which is due to the closer packing of the CO_2 molecules under the higher pressure in the relatively narrow pores. Hence, the behavior of the total Q_{st} is the result of the two cooperative contributions. The increasing contribution from the CO_2···CO_2 interactions indicates that the CO_2 clusters could have formed inside the pores. Hence, GCMC simulation was used to investigate the potential CO_2 clusters. Some small CO_2 clusters can be found in the snapshot at 195 K and low pressure (~ 21 Pa) calculated using the GCMC method (Supplementary Fig. 11), but at 273 K, similar CO_2 clusters can only be observed under a relatively high pressure of 11 kPa. The snapshots of the framework of **FJI-H14** with CO_2 molecules adsorbed are shown in Fig. 5a. The weak interactions between neighboring CO_2 molecules are found in terms of the short C···O separation (from 2.71 to 3.50 Å) for adjacent CO_2 molecules,

Table 1 Cyclic carbonates from epoxides and CO_2[a]

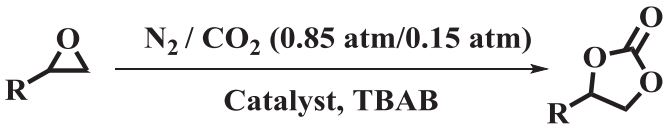

Entry	Substrates	Catalysts	t[h]	Yield(%)[b]
1	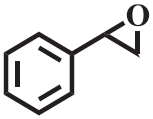	**FJI-H14**	24	86
2	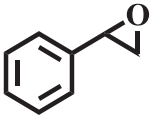	–	24	52
3	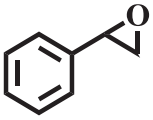	$Cu(OAc)_2$	24	45[c]
4	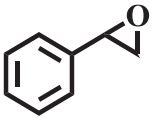	$Cu(NO_3)_2$+ H_2BTTA	24	70
5	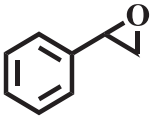	HKUST-1	24	67
6	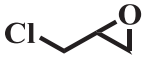	**FJI-H14**	24	95
7	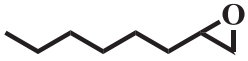	**FJI-H14**	24	27

[a]Reaction conditions: styrene oxide (20.0 mmol), catalyst (0.48 mol% per Cu(II) units), TBAB (2.5 mol%) in a Schleck tube with condenser, 1 atm simulated post-combustion flue (CO_2 = 0.15 atm, N_2 = 0.85 atm) was bubbled at 80 °C for 24 h
[b]Determined by ^1H NMR.
[c]Some by-products were found when $Cu(OAc)_2$ was used as a catalyst

which links those CO_2 molecules into small clusters (Fig. 5b and Supplementary Fig. 12).

To verify the preferential adsorption sites experimentally, in situ fourier transform infrared microscope (FT-IR) spectra of activated **FJI-H14** sample have been collected at increasing equilibrium pressure under a CO_2 atmosphere. Figure 4b shows the background-subtracted IR spectra obtained by the progressive lowering of equilibrium pressure at room temperature. The strong absorption bands at 2,340 and 2,328 cm^{-1} red-shifted by $\Delta\nu$ of about −9 and −21 cm^{-1} from gas phase CO_2 asymmetric stretch (ν_{as} = 2349 cm^{-1}) might be attributed to the ν_{as} mode of CO_2 (Supplementary Fig. 13) interacting with Cu(II) centers. The slightly blue-shifted band at 2,361 cm^{-1} ($\Delta\nu$ = + 12 cm^{-1} shift) can be readily assigned to the asymmetric ν_{as} stretch of CO_2 interacting with the exposed Lewis base sites throughout the channel. On the low-frequency side of this main absorption, the less intense bands at 2,275 cm^{-1} result from the interaction between Cu(II) center and $^{13}CO_2$ which is present (1%) naturally in $^{12}CO_2$. The stronger absorption bands at 2,340 cm^{-1} and 2,328 cm^{-1} also indicate that CO_2 molecules tend to stack around the open Cu(II) sites, which is in accord with the above theoretical calculation.

Large-scale synthesis. For practical applications, efficient macroscopic preparation and purification are a bottleneck problem which must be solved. After many attempts, the following protocol for large-scale preparation of **FJI-H14** has been established: by directly mixing H_2BTTA ligand and $Cu(NO_3)_2$ in water and then refluxing for 1 day, microcrystalline **FJI-H14** can be obtained with a high yield of 90%, its purity confirmed by PXRD analysis (Fig. 6b). Scanning electron microscopy measurements demonstrate that the relatively uniform rod crystallites form on the scale of about 20 μm, displaying a similar morphology with the single crystal (Fig. 6a) obtained from the hydrothermal reaction. Therefore, macroscopic samples of **FJI-H14** even on a 10 g scale can be readily synthesized by this method, which makes its application more possible.

Catalyzed cycloaddition of CO_2 using flue gas as feedstock. Another attractive means of effective elimination of CO_2 is the direct chemical conversion of CO_2 into value-added chemicals, such as dimethyl carbonate, cyclic carbonates, *N*,*N*'-disubstituted ureas or formic acid. Given their wide applications in the pharmaceutical and fine chemical industries, cyclic carbonates formed by the coupling of epoxides with CO_2 have attracted intense interest. Although several existing MOFs have been shown to be excellent heterogeneous Lewis acid catalysts for chemical conversion of CO_2 either at high pressure or normal pressure[53–56], the exploration of practically useful MOF materials which can catalyze the conversion of CO_2 obtained directly from power plants remains a challenge to be addressed. The high density of OMSs and LBSs which are finely distributed throughout the channel pores of **FJI-H14**, are devoted to capturing CO_2 effectively and selectively under ambient conditions. Such unusual synergistic effects may also improve chemical conversion of post-combustion CO_2 from the power plant. Here, we use a mixed gas which contains 0.15 atm CO_2 and 0.85 atm N_2 to simulate flue gas from the power plant. As expected, **FJI-H14** displays a much higher catalytic activity for cycloaddition of styrene oxide with the simulated flue gas than other catalysts, such as homogeneous $Cu(OAc)_2$, heterogeneous HKUST-1 and a mixture of $Cu(NO_3)_2$ and free H_2BTTA ligand. As shown in Table 1, absence of extra Lewis acid catalysts only lead to a moderate yield (52%), while use of extra Cu(II) catalyst can improve their reaction activity, with the exception of $Cu(OAc)_2$. Catalyzed by **FJI-H14**, chemical conversion of diluted CO_2 with styrene oxide into corresponding cyclic carbonates gives a yield of 86% within 24 h, while use of homogeneous $Cu(OAc)_2$ and the mixture of $Cu(NO_3)_2$ and H_2BTTA leads only to 45 and 70% yields respectively under the same reaction conditions. Further tests demonstrate that the **FJI-H14** is more active than well-known HKUST-1 which leads to only 67% yield under the same conditions. All these results indicate that **FJI-H14** is indeed an efficient catalyst for chemical conversion of CO_2 under practical conditions. In order to investigate the catalytic character of **FJIH-14**, another two different sized substrates have been selected. As shown in Table 1 entries 5–6, the smaller (chloromethyl)ethylene oxide gives a higher yield (95%), while 1,2-epoxyoctane leads to a lower yield (27%), indicating that the cycloaddition reaction may occur within the pores of **FIJ-H14**, into which smaller-sized substrates could easily diffuse and make contact with the active sites. To further prove that the reaction may occur in the pores of **FJI-H14**, uptake of different reactants has also been assessed. Further analysis demonstrates that (chloromethyl)ethylene oxide indeed diffuses into the pores of **FJI-H14** more easily than 1,2-epoxyoctane and styrene oxide which apparently have similar diffusion rates. Considering the similar diffusion from 1,2-epoxyoctane and styrene oxide, the higher activity of styrene oxide compared to 1,2-epoxyoctane may result from following two factors: first, a phenyl ring is an electron-withdrawing group, which can improve reaction activity, and second, the π–π interaction from the phenyl ring of styrene oxide and the aromatic rings of the **FJI-H14** framework also can improve reaction activity. This may provide a strategy for development of more practical catalysts for the conversion of CO_2 directly from flue gas.

Discussion

Considering that most of CO_2 emission is generated from power stations, direct elimination of such CO_2 should play an important role in the reduction of global CO_2 emissions. The characteristics and composition of post-combustion CO_2 determine that an ideal adsorbent for post-combustion CO_2 capture should possess advantages such as high CO_2 uptake and selectivity at ambient pressure, excellent chemical stability and thermal stability, good reusability and large-scale production with low cost. Porous MOFs have been proved to be effective adsorbents for CO_2 capture due to their large capacity for the adsorption of gases, but development of an ideal MOF for post-combustion CO_2 capture is still challenging. Although many different OMS and LBS have been introduced into MOFs to improve CO_2 capture, only very few porous MOFs have been realized for high CO_2 capture at ambient conditions, and most of them are sensitive to water. **FJI-H14** not only shows extraordinary high volumetric uptake of CO_2 with high selectivity under ambient conditions but is also highly resistant to water and an acid/base environment; furthermore, it also can be reused without loss of adsorption capacity and prepared on a large-scale with low cost. These advantages make **FJI-H14** an ideal and practical adsorbent for post-combustion CO_2. An unusual synergistic effect from multiple active sites has also been observed, and may provide a strategy for the design of more effective adsorbents for CO_2 capture. Further chemical conversion of captured CO_2 to high-value products, such as cyclic carbonate, is also attractive, and several existing MOFs have been proved to be excellent heterogeneous Lewis acid catalysts for chemical conversion of pure CO_2. However, development of MOF materials which can catalyze the direct conversion of post-combustion CO_2 still remains a challenge. It is shown here that **FJI-H14** can directly and smoothly catalyze the chemical transformation of simulated post-combustion gas CO_2 into corresponding cyclic carbonates. All these results should be instructive for the design and discovery of more effective and practical MOF materials for the elimination of post-combustion CO_2 in the near future.

Methods

Synthesis and scale up. A mixture of $Cu(NO_3)_2{\cdot}3H_2O$ (0.05 mmol, 12 mg) and H_2BTTA (0.05 mmol, 15 mg) in H_2O (4 ml) was sealed in a 23 mL Teflon vial, which was heated at 120 °C for 3 days, then cooled to room temperature. After washing with fresh acetone, blue crystals of **FJI-H14** were obtained in 73% yield based on the organic ligand H_2BTTA. Elemental analysis was calculated for **FJI-H14**: C, 29.54%; H, 4.13%; N, 17.23%. Found: C, 29.35%; H, 4.12%; N, 17.29%. For scale up, a mixture of $Cu(NO_3)_2{\cdot}3H_2O$ (1 mmol, 241.6 mg) and H_2BTTA (1 mmol, 300.1 mg) in H_2O (80 ml) was refluxed for 1 day, and then the blue powder of **FJI-H14** microcrystals could be obtained in 90% yield based on H_2BTTA. After three washings with water and two with acetone, the phase purity of the sample was confirmed by PXRD.

Characterization. Elemental analyses for C, H, N were carried out on a German Elementary Vario EL III instrument. The ^{1}H NMR spectra were measured on an AVANCE III Bruker Biospin spectrometer, operating at 400 MHz. Thermogravimetric analyses (TGA) were recorded on an NETZSCH STA 449 C unit at a heating rate of 10 °C min^{-1} under flowing nitrogen atmosphere. In situ FT-IR spectra were obtained using a NICOLET 6700 instrument at 298 K. The PXRD patterns were collected using a Rigaku MiniFlex 600 X-ray diffractometer with monochromatic Cu Kα radiation (λ = 1.54 Å). Simulations of the PXRD spectrum were carried out by the single-crystal data and diffraction-crystal module of the

Mercury program, available free of charge via the internet at https://www.ccdc.cam.ac.uk/solutions/csd-system/components/mercury/.

Single-crystal X-ray diffraction. The single-crystal data of **FJI-H14** was collected on a SuperNova diffractometer at 100 K. The structure was solved using *SHELXT*-2014 and refined by full-matrix least squares on F^2 with *SHELXL*-2014[57]. All the non-hydrogen atoms were refined anisotropically. Hydrogen atoms of the organic ligands were generated theoretically onto the specific atoms and refined isotropically. We employed *PLATON/SQUEEZE*[58] to calculate the contribution to the diffraction from the solvent region and thereby produced a set of solvent-free diffraction intensities. The final formula was calculated from the SQUEEZE results combined with elemental analysis data and TGA data. Crystallographic data and structure refinement parameters for this crystal are summarized in Supplementary Table 1.

Gas-adsorption. Low-pressure (<1 bar) adsorption measurements were performed using an Accelerated Surface Area and Porosimetry 2020-M System. Before the measurements, about 100 mg solvent-exchanged samples were loaded into the sample tube and then degassed under dynamic vacuum at 100 °C for 10 h to obtain fully desolvated samples. Low-pressure N_2 adsorption isotherms were measured at 77 K in a liquid nitrogen bath (Supplementary Fig. 6). Low-pressure CO_2 adsorption isotherms were measured at 195, 273, 283, 288, 291, 293, 298 and 308 K. The specific surface areas were determined using the BET model from the CO_2 adsorption isotherm.

The isosteric heat of adsorption. Method 1: the isosteric heat of adsorption Q_{st} was calculated using the Clausius–Clapeyron equation (equation (1)).

$$\ln(P_i) = Q_{st} \times \frac{1}{RT_i} + C, \quad (1)$$

where P_i is the pressure of the isotherm i (kPa), T_i is the temperature of isotherm i (K), R is the gas constant and C is a constant. The Qst is subsequently obtained from the slope of plots of $\ln(P_i)$ as a function of 1/T (Supplementary Fig. 7 and Supplementary Table 4).

Method 2: the Qst was estimated from isotherms at different temperatures applying the Virial fitting method (equation (2) and Supplementary Fig. 8). The fitting parameters were then used to calculate the Q_{st} using equation (3).

$$\ln P = \ln N + \frac{1}{T}\sum_{i=0}^{m} a_i N^i + \sum_{i=0}^{n} b_i N^i, \quad (2)$$

$$Q_{st} = -R\sum_{i=0}^{m} a_i N^i, \quad (3)$$

where P is the pressure (mmHg), N is the adsorbed quantity (mg g^{-1}), T is the temperature (K), R is the gas constant, a_i and b_i are virial coefficients and m and n represent the number of coefficients required to adequately describe the isotherms (herein, $m = 5$, $n = 2$).

Calculation of gas selectivity based on IAST. The gas adsorption isotherms were first fitted to a Langmuir-Freundlich model. IAST starts from the Raoults' Law type of relationship between fluid and adsorbed phase.

$$P_i = Py_i = P_i^0 x_i, \quad (4)$$

$$\sum_{i=1}^{n} x_i = \sum_{i=1}^{n} \frac{P_i}{P_i^0} = 1, \quad (5)$$

where P_i is the partial pressure of component i (kPa), P is the total pressure (kPa), y_i and x_i represent mole fractions of component i in gas and adsorbed phase (dimensionless). P_i^0 is the equilibrium vapor pressure (kPa).

In IAST, P_i^0 is defined by relating to spreading pressure π,

$$\frac{\pi S}{RT} = \int_0^{P_i^0} \frac{q_i(P_i)}{P_i} dP_i = \Pi \text{ (Constant)}, \quad (6)$$

where π is the spreading pressure, S is the specific surface area of adsorbent (m^2 g^{-1}), R is the gas constant, T is the temperature (K) and $q_i(P_i)$ is the single component equilibrium obtained from the isotherm (mg g^{-1}).

The isotherm parameters are known from the previous fitting. The adsorption selectivities S_{ads} were calculated using equation (7).

$$S_{ads} = \frac{q_1/q_2}{p_1/p_2}. \quad (7)$$

In this study, IAST calculations were carried out assuming CO_2/N_2 (15/85) binary mixed gases at 298 K and pressure up to 1 bar to mimic the composition and condition of flue gas for post-combustion CO_2 capture.

Computational methodologies. The GCMC simulations for CO_2 at 195, 273 and 298 K and up to 100 kPa were performed using with *RASPA* v2.03[59]. The **FJI-H14s** framework was generated in the *R*3 space group based on the crystallographic data of **FJI-H14** to avoid disorder in the structure (Supplementary Fig. 14). Twelve unit cells of **FJI-H14s** (2 × 2 × 3) were used to construct the simulation box of the GCMC run. The structural parameters of simulation box are $a = b = 44.9714$ Å and $c = 33.1527$ Å, as well as $\alpha = \beta = 90°$ and $\gamma = 120°$. The partial charges on the framework atoms were calculated by the Gaussian09 software at the B3LYP/6–31 G* level of theory[60]. Partial atomic charges were extracted using the ChelpG method by fitting them to reproduce the electrostatic potential generated by the DFT calculations. The charge was adjusted slightly in order to result in a neutral framework. Resulting partial charges for **FJI-H14s** are given in Supplementary Table 5.

CO_2–CO_2 and CO_2-framework interactions were calculated using a Lennard–Jones (LJ) + Coulomb potential. LJ parameters for the framework atoms were taken from the Dreiding Force Field except for the copper atom, for which the parameters were taken from UFF (Supplementary Table 7). The CO_2 LJ parameters were taken from an empirical TraPPE force field with a partial charge on each atom (Supplementary Table 6). The mixing LJ parameters between different atomic types were calculated according to the Lorentz–Berthelot mixing rule. Lorentz–Berthelot mixing rules were used for all cross terms, and LJ interactions beyond 12.8 Å were neglected. The Ewald sum method was used to compute the electrostatic interactions. The fugacity of CO_2 was calculated using the Peng-Robinson equation of state with the corresponding parameters. Simulations for CO_2 adsorption used 100,000 cycles for equilibration and 100,000 cycles for data collection. In a cycle, N Monte Carlo moves were performed, where N is whichever value is larger between 20 and the number of molecules in the system. Monte Carlo moves used with equal probability were translation, rotation, insertion, deletion, and random reinsertion of an existing molecule at a new position, while framework atoms remained fixed at their original positions.

The simulated isosteric heats of adsorption are computed from the GCMC simulations using the expression (equation (8)).

$$Q_{st} = RT - \frac{\langle U_{gg}N\rangle - \langle U_{gg}\rangle\langle N\rangle}{\langle N^2\rangle - \langle N\rangle^2} - \frac{\langle U_{gf}N\rangle - \langle U_{gf}\rangle\langle N\rangle}{\langle N^2\rangle - \langle N\rangle^2}, \quad (8)$$

where the brackets ⟨ ⟩ denote the ensemble average, R is the gas constant, N is the number of gas molecules in the system, U_{gg} is gas···gas interaction energy and U_{gh} is the gas···framework interaction energy. The second and third terms are the contributions to the simulated Q_{st} from the gas···gas interaction and the gas···framework interaction, respectively.

DFT methods help shed light on adsorption mechanisms by calculating the adsorption energy of CO_2 in MOF. Three possible main adsorption sites for adsorbed CO_2 in MOF were investigated by the Dmol[3] module integrated into the Material Studio 7.0 program package[61]. The PBE-type exchange-correlation functional[62] with a generalized gradient approximation and the Double Numerical plus polarization (DNP) basis sets[63] that include a d-type polarization function on all non-hydrogen atoms and a p-type polarization function on all hydrogen atoms were employed for all calculations[64]. The FINE quality mesh size was employed in the calculations. During the CO_2-MOF structure optimization, the lattice parameters and the atomic fraction positions of the MOF crystal were kept immobile and the single CO_2 molecule was allowed to move during optimization. The possible adsorption sites are shown in the Fig. 4d–f. The adsorption energies were calculated in terms of equation (9)

$$E_{ads} = E_{MOF-CO_2} - E_{MOF} - E_{CO_2}, \quad (9)$$

where E_{MOF-CO_2} stands for the energy of the optimized adsorbate-MOF structure, and E_{MOF}, and E_{CO2} denote the energies of the bare MOF structure and the isolated CO_2 molecule, respectively. According to this equation, a more negative adsorption energy means more favorable binding.

Catalyzation of cycloaddition of simulated post-combustion CO_2. 20 mmol styrene oxide, 0.48 mol% per Cu(II) units (for example, 18 mg activated **FJI-H14** (0.016 mmol), 8.7 mg $Cu(OAc)_2$ (0.048 mmol)), and 164 mg TBAB (0.5 mmol, 2.5 mol%) were placed in a 5 mL dry Schleck tube with condenser, then 1 atm simulated post-combustion flue gas (CO_2 = 0.15 atm, N_2 = 0.85 atm) was introduced by bubbling, and the reaction mixture was stirred at 80 °C for 24 h.

Uptake of different reactants. 10 mg of activated crystals of **FJI-H14** was placed in a dry 5 ml Schleck flask, the flask was then evacuated under dynamic vacuum at 80 °C for 2 h and filled with argon, then 1 ml reactant was injected and the reaction was kept under argon atmosphere. 10 min later, the inclusion crystals of **FJI-H14** were filtered, after removing surface reactant molecules; the inclusion reactants can be readily removed from inclusion crystals **FJI-H14** by ultrasonic processing in DMSO-d^6 solution and further determined by ^{1}H NMR. Finally, about 2.78 μmol

of (chloromethyl)ethylene oxide, 1.2 μmol of 1,2-epoxyoctane, or 1.1 μmol of styrene oxide were added.

Data availability. The X-ray crystallographic coordinates for structure reported in this article have been deposited at the Cambridge Crystallographic Data Centre (CCDC), under deposition number CCDC 1517725. These data can be obtained free of charge from The Cambridge Crystallographic Data Centre via www.ccdc.cam.ac.uk/data_request/cif.

Received: 5 January 2017 Accepted: 22 August 2017
Published online: 01 November 2017

References

1. Watts, R. G. *Global Warming and the Future of the Earth* (Morgan & Claypool Publishers, Denver, 2007).
2. Wang, Q. A., Luo, J. Z., Zhong, Z. Y. & Borgna, A. CO_2 capture by solid adsorbents and their applications: current status and new trends. *Energy Environ. Sci.* **4**, 42–55 (2011).
3. Liu, J., Thallapally, P. K., McGrail, B. P., Brown, D. R. & Liu, J. Progress in adsorption-based CO_2 capture by metal-organic frameworks. *Chem. Soc. Rev.* **41**, 2308–2322 (2012).
4. Metz, B., Davidson, O. R., Bosch, P. R., Dave, R. & Meyer, L. A. IPCC. *Fourth Assessment Report* (Intergovernmental Panel on Climate Change, 2007).
5. Sumida, K. et al. Carbon dioxide capture in metal-organic frameworks. *Chem. Rev.* **112**, 724–781 (2012).
6. Zhang, Z., Yao, Z.-Z., Xiang, S. & Chen, B. Perspective of microporous metal–organic frameworks for CO_2 capture and separation. *Energy Environ. Sci.* **7**, 2868–2899 (2014).
7. Li, J. R. et al. Carbon dioxide capture-related gas adsorption and separation in metal-organic frameworks. *Coord. Chem. Rev.* **255**, 1791–1823 (2011).
8. Bezuidenhout, C. X., Smith, V. J., Bhatt, P. M., Esterhuysen, C. & Barbour, L. J. Extreme carbon dioxide sorption hysteresis in open-channel rigid metal-organic frameworks. *Angew Chem. Int. Ed. Engl.* **54**, 2079–2083 (2015).
9. Chen, K. J. et al. Tuning pore size in square-lattice coordination networks for size-selective sieving of CO_2. *Angew Chem. Int. Ed. Engl.* **55**, 10268–10272 (2016).
10. Kajiwara, T. et al. Photochemical reduction of low concentrations of CO_2 in a porous coordination polymer with a ruthenium(II)-CO complex. *Angew Chem. Int. Ed. Engl.* **55**, 2697–2700 (2016).
11. Kumar, A. et al. Direct air capture of CO_2 by physisorbent materials. *Angew Chem. Int. Ed. Engl.* **54**, 14372–14377 (2015).
12. Mottillo, C. & Friscic, T. Carbon dioxide sensitivity of zeolitic imidazolate frameworks. *Angew Chem. Int. Ed. Engl.* **53**, 7471–7474 (2014).
13. Vaidhyanathan, R. et al. Competition and cooperativity in carbon dioxide sorption by amine-functionalized metal-organic frameworks. *Angew Chem. Int. Ed. Engl.* **51**, 1826–1829 (2012).
14. Yang, Q. et al. A water stable metal-organic framework with optimal features for CO_2 capture. *Angew Chem. Int. Ed. Engl.* **52**, 10316–10320 (2013).
15. Li, M., Li, D., O'Keeffe, M. & Yaghi, O. M. Topological analysis of metal-organic frameworks with polytopic linkers and/or multiple building units and the minimal transitivity principle. *Chem. Rev.* **114**, 1343–1370 (2014).
16. Bai, Y. et al. Zr-based metal-organic frameworks: design, synthesis, structure, and applications. *Chem. Soc. Rev.* **45**, 2327–2367 (2016).
17. Liu, Y., Wang, Z. U. & Zhou, H.-C. Recent advances in carbon dioxide capture with metal-organic frameworks. *Greenhouse Gas Sci. Technol.* **2**, 239–259 (2012).
18. Fracaroli, A. M. et al. Metal-organic frameworks with precisely designed interior for carbon dioxide capture in the presence of water. *J. Am. Chem. Soc.* **136**, 8863–8866 (2014).
19. Liao, P. Q. et al. Strong and dynamic CO_2 sorption in a flexible porous framework possessing guest chelating claws. *J. Am. Chem. Soc.* **134**, 17380–17383 (2012).
20. Zhang, Z. et al. Polymer-metal-organic frameworks (polyMOFs) as water tolerant materials for selective carbon dioxide separations. *J. Am. Chem. Soc.* **138**, 920–925 (2016).
21. Yang, S. et al. Selectivity and direct visualization of carbon dioxide and sulfur dioxide in a decorated porous host. *Nat. Chem.* **4**, 887–894 (2012).
22. Zhang, Z., Zhao, Y., Gong, Q., Li, Z. & Li, J. MOFs for CO_2 capture and separation from flue gas mixtures: the effect of multifunctional sites on their adsorption capacity and selectivity. *Chem. Commun.* **49**, 653–661 (2013).
23. Wilmer, C. E., Farha, O. K., Bae, Y.-S., Hupp, J. T. & Snurr, R. Q. Structure–property relationships of porous materials for carbon dioxide separation and capture. *Energy Environ. Sci.* **5**, 9849–9856 (2012).
24. Mason, J. A. et al. Application of a high-throughput analyzer in evaluating solid adsorbents for post-combustion carbon capture via multicomponent adsorption of CO_2, N_2, and H_2O. *J. Am. Chem. Soc.* **137**, 4787–4803 (2015).
25. Lin, Q., Wu, T., Zheng, S. T., Bu, X. & Feng, P. Single-walled polytetrazolate metal-organic channels with high density of open nitrogen-donor sites and gas uptake. *J. Am. Chem. Soc.* **134**, 784–787 (2012).
26. Zheng, B., Bai, J., Duan, J., Wojtas, L. & Zaworotko, M. J. Enhanced CO_2 binding affinity of a high-uptake rht-type metal-organic framework decorated with acylamide groups. *J. Am. Chem. Soc.* **133**, 748–751 (2011).
27. Yan, Y. et al. Modulating the packing of $[Cu_{24}(isophthalate)_{24}]$ cuboctahedra in a triazole-containing metal–organic polyhedral framework. *Chem. Sci.* **4**, 1731–1736 (2013).
28. Qin, J.-S. et al. N-rich zeolite-like metal–organic framework with sodalite topology: high CO_2 uptake, selective gas adsorption and efficient drug delivery. *Chem. Sci.* **3**, 2114–2118 (2012).
29. McDonald, T. M. et al. Capture of carbon dioxide from air and flue gas in the alkylamine-appended metal-organic framework mmen-Mg_2(dobpdc). *J. Am. Chem. Soc.* **134**, 7056–7065 (2012).
30. McDonald, T. M., D'Alessandro, D. M., Krishna, R. & Long, J. R. Enhanced carbon dioxide capture upon incorporation of N,N′-dimethylethylenediamine in the metal–organic framework CuBTTri. *Chem. Sci.* **2**, 2022–2028 (2011).
31. Liao, P.-Q. et al. Putting an ultrahigh concentration of amine groups into a metal–organic framework for CO_2 capture at low pressures. *Chem. Sci.* **7**, 6528–6533 (2016).
32. Lee, W. R. et al. Exceptional CO_2 working capacity in a heterodiamine-grafted metal–organic framework. *Chem. Sci.* **6**, 3697–3705 (2015).
33. Sarkisov, L. & Harrison, A. Computational structure characterisation tools in application to ordered and disordered porous materials. *Mol. Simulat.* **37**, 1248–1257 (2011).
34. Wang, B. et al. Highly stable Zr(IV)-based metal-organic frameworks for the detection and removal of antibiotics and organic explosives in water. *J. Am. Chem. Soc.* **138**, 6204–16 (2016).
35. Lv, X. L. et al. A base-resistant metalloporphyrin metal-organic framework for C-H Bond HALOGENATION. *J. Am. Chem. Soc.* **139**, 211–217 (2016).
36. Liao, P.-Q. et al. Monodentate hydroxide as a super strong yet reversible active site for CO_2 capture from high-humidity flue gas. *Energy Environ. Sci.* **8**, 1011–1016 (2015).
37. Wang, K. et al. Pyrazolate-based porphyrinic metal-organic framework with extraordinary base-resistance. *J. Am. Chem. Soc.* **138**, 914–919 (2016).
38. Colombo, V. et al. High thermal and chemical stability in pyrazolate-bridged metal–organic frameworks with exposed metal sites. *Chem. Sci.* **2** 1311–1319 (2011).
39. Caskey, S. R., Wong-Foy, A. G. & Matzger, A. J. Dramatic tuning of carbon dioxide uptake via metal substitution in a coordination polymer with cylindrical pores. *J. Am. Chem. Soc.* **130**, 10870–10871 (2008).
40. Millward, A. R. & Yaghi, O. M. Metal-organic frameworks with exceptionally high capacity for storage of carbon dioxide at room temperature. *J. Am. Chem. Soc.* **127**, 17998–17999 (2005).
41. Xiang, S. et al. Microporous metal-organic framework with potential for carbon dioxide capture at ambient conditions. *Nat. Commun.* **3**, 954 (2012).
42. Nugent, P. et al. Porous materials with optimal adsorption thermodynamics and kinetics for CO_2 separation. *Nature* **495**, 80–84 (2013).
43. Nugent, P. S. et al. A robust molecular porous material with high CO_2 uptake and selectivity. *J. Am. Chem. Soc.* **135**, 10950–10953 (2013).
44. An, J., Geib, S. J. & Rosi, N. L. High and selective CO_2 uptake in a cobalt adeninate metal-organic framework exhibiting pyrimidine- and amino-decorated pores. *J. Am. Chem. Soc.* **132**, 38–39 (2010).
45. Li, B. et al. Enhanced binding affinity, remarkable selectivity, and high capacity of CO_2 by dual functionalization of a rht-type metal-organic framework. *Angew Chem. Int. Ed. Engl.* **51**, 1412–1415 (2012).
46. Li, J.-R. et al. Porous materials with pre-designed single-molecule traps for CO_2 selective adsorption. *Nat. Commun.* **4**, 1538 (2013).
47. Chen, S.-S. et al. Temperature dependent selective gas sorption of the microporous metal-imidazolate framework [Cu(L)] [H_2L=1,4-di(1H-imidazol-4-yl)benzene]. *Chem. Commun.* **47**, 752–754 (2011).
48. Zhao, X. et al. Multivariable modular design of pore space partition. *J. Am. Chem. Soc.* **138**, 15102–15105 (2016).
49. Wang, H. et al. A flexible microporous hydrogen-bonded organic framework for gas sorption and separation. *J. Am. Chem. Soc.* **137**, 9963–9970 (2015).
50. Rowsell, J. L. C. & Yaghi, O. M. Effects of functionalization, catenation, and variation of the metal oxide and organic linking units on the low-pressure hydrogen adsorption properties of metal–organic frameworks. *J. Am. Chem. Soc.* **128**, 1304–1315 (2006).
51. Myers, A. L. & Prausnitz, J. M. Thermodynamics of mixed-gas adsorption. *AIChE J.* **11**, 121–127 (1965).
52. Luo, F. et al. UTSA-74: A MOF-74 isomer with two accessible binding sites per metal center for highly selective gas separation. *J. Am. Chem. Soc.* **138**, 5678–5684 (2016).
53. Zhou, Z., He, C., Xiu, J., Yang, L. & Duan, C. Metal-organic polymers containing discrete single-walled nanotube as a heterogeneous catalyst for the cycloaddition of carbon dioxide to epoxides. *J. Am. Chem. Soc.* **137**, 15066–15069 (2015).

54. He, H., Perman, J. A., Zhu, G. & Ma, S. Metal-organic frameworks for CO_2 chemical transformations. *Small* **12**, 6309–6324 (2016).
55. Gao, W. Y. et al. Crystal engineering of an nbo topology metal-organic framework for chemical fixation of CO_2 under ambient conditions. *Angew Chem. Int. Ed. Engl.* **53**, 2615–2619 (2014).
56. Xie, Y., Wang, T. T., Liu, X. H., Zou, K. & Deng, W. Q. Capture and conversion of CO_2 at ambient conditions by a conjugated microporous polymer. *Nat. Commun.* **4**, 1960 (2013).
57. Sheldrick, G. M. Crystal structure refinement with SHELXL. *Acta Crystallogr. C Cryst. Struct. Commun.* **71**, 3–8 (2015).
58. Spek, A. L. PLATON SQUEEZE: a tool for the calculation of the disordered solvent contribution to the calculated structure factors. *Acta Crystallogr. C Cryst. Struct. Commun.* **71**, 9–18 (2015).
59. Dubbeldam, D., Calero, S., Ellis, D. E. & Snurr, R. Q. RASPA: molecular simulation software for adsorption and diffusion in flexible nanoporous materials. *Mol. Simulat.* **42**, 81–101 (2015).
60. Frisch, M. J. et al. Gaussian 09 Revision B01 (Gaussian Inc, 2009).
61. Materials Studio version 7.0, Accelrys Inc, (San Diego, USA 2013).
62. Perdew, J. P., Burke, K. & Ernzerhof, M. Generalized gradient approximation made simple. *Phys. Rev. Lett.* **77**, 3865–3868 (1996).
63. Delley, B. An all-electron numerical method for solving the local density functional for polyatomic molecules. *J. Chem. Phys.* **92**, 508–517 (1990).
64. Yang, Q. & Zhong, C. Understanding hydrogen adsorption in metal–organic frameworks with open metal sites: A computational study. *J. Phys. Chem. B.* **110**, 655–658 (2006).

Acknowledgements

Dedicated to professor Xin-Tao Wu on the ocassion of his 80th birthday. This work was supported by 'Strategic Priority Research Program' of the Chinese Academy of Sciences (XDB20000000, XDA09030102), National Key R&D Program of China (2016YFB0600903), the 973 Program (2014CB932101, 2013CB933200), the National Natural Science Foundation of China (21390392, 21131006 and 21471148), and the Youth Innovation Promotion Association CAS.

Author contributions

Q.C., D.Y. and M.H. conceived and designed the experiments and co-wrote the paper. L.L. performed most of the experiments and analyzed data. C.L. worked on all computational simulations. H.X., J.Q. and L.Z. performed adsorption test. Q.C., D.Y., J.F., H. J., M.H. and L.L. analyzed the data and wrote the manuscript. All authors discussed the results and commented on the manuscript.

Additional information

Supplementary Information accompanies this paper at doi:10.1038/s41467-017-01166-3.

Competing interests: The authors declare no competing financial interests.